Research Article | Vol. 32, No. 22 / 21 Oct 2024 / Optics Express 39560
Optics EXPRESS

Mid-infrared silicon photonic lasers based on GeSn slab waveguide on silicon

YIN-PU HUANG,[1,2] BO-RUI WU,[1,2] SOUMAVA GHOSH,[2] YUE-TONG JHENG,[2] YA-LUN HO,[3] YEN-JU WU,[4] ATTAPORN WISESSINT,[5] MUNHO KIM,[6] AND GUO-EN CHANG[1,2,*]

[1]*Graduate Institute of Opto-Mechatronics, National Chung Cheng University, Chiayi County 621301, Taiwan*
[2]*Department of Mechanical Engineering and Advanced Institute of Manufacturing with Hi-Tech Innovations (AIM-HI), National Chung Cheng University, Chiayi County 621301, Taiwan*
[3]*Research Center for Electronic and Optical Materials, National Institute for Materials Science, Tsukuba 305-0044, Ibaraki, Japan*
[4]*Center for Basic Research on Materials, National Institute for Materials Science, Tsukuba 305-0047, Ibaraki, Japan*
[5]*Department of Mechanical Engineering, Kasetsart University, Bangkok 10900, Thailand*
[6]*School of Electrical and Electronic Engineering, Nanyang Technological University, Singapore 639798, Singapore*
[*]*imgec@ccu.edu.tw*

Abstract: GeSn alloy has emerged as an attractive active material for Si-based mid-infrared (MIR) lasers due to its direct bandgap nature at higher Sn concentrations. Here, we report on an optically-pumped GeSn MIR lasers based on planar slab waveguide with a top Si ridge structure. The inclusion of 10% Sn transforms the GeSn active layer into a direct bandgap material. The Si ridge structure ensures appropriate optical confinements with reduced scattering loss from the waveguide sidewall. Lasing action was achieved under optical pumping with a low threshold of 60.85 kW/cm^2 and an emission wavelength of 2238 nm at $T = 40$ K. Lasing action was also observed up to $T = 90$ K with a threshold of 170 kW/cm^2.

1. Introduction

Silicon photonics operating in the mid-infrared (MIR) range of 2–20 μm has been increasingly recognized for its potential in applications such as chemical analysis, bio-medical diagnosis, free-space communications, and spectroscopy [1,2]. MIR silicon photonic chips necessitate the integration of various photonic devices on a single Si chip, manufactured using complementary metal-oxide semiconductor (CMOS) technology. Although various Si-based passive and active photonic devices capable of operation in the MIR region have been demonstrated [3], the indirect bandgap nature of Si limits the efficiency of Si-based light emitters, hindering the completion of MIR silicon photonics. Over the past two decades, the development of high-quality group-IV GeSn alloys on Si substrates with suitable buffer layers through low-temperature molecular beam epitaxy (MBE) and chemical vapor deposition (CVD) techniques has opened new avenues for efficient light emitters in MIR silicon photonics [4–6]. With a quasi-direct bandgap nature, Ge has a direct-band (Γ-valley) conduction band (CB) of only 136.5 meV above the lowest indirect-band (L-valley) CB [7]; the incorporation of α-Sn, another group-IV material, can significantly reduce this energy, transforming the material into a direct-gap material with a sufficiently high Sn content (> 7%) [8]. This reduction in the direct bandgap also extends the emission wavelength into the MIR region [9]. Moreover, a unique momentum (k)-space separation owing to the close proximity of Γ- and L-valley CB enhances the optical performance of GeSn-based devices

#540223 https://doi.org/10.1364/OE.540223
Journal © 2024 Received 23 Aug 2024; revised 2 Oct 2024; accepted 2 Oct 2024; published 15 Oct 2024

Optics EXPRESS

[10,11]. Furthermore, the compatibility with standard Si-CMOS technology, and the potential for monolithic integration on the same Si chip have rendered GeSn a promising candidate for light emitters and enabled a reduction in fabrication costs.

With the successful growth of direct-bandgap GeSn alloys, the first optically pumped GeSn laser with 12.6% Sn was achieved with a threshold of 325 kW/cm^2 up to $T = 100$ K [12]. Subsequent research has continued to improve the performance of optically pumped GeSn lasers in terms of operating temperatures and thresholds [13–22]. Recent advancements include room-temperature GeSn optically pumped lasers [23,24] and GeSn-based electrically injected lasers up to 140 K [9,25–28]. These developments have established GeSn lasers as viable light sources for MIR silicon photonics. However, the performance of GeSn lasers still falls short of the commercially available III-V-based lasers [29–31] in terms of the threshold and operating temperature, thus necessitating further improvements to meet practical application demands.

Optical loss in semiconductor lasers is crucial for performance, and is attributed mainly to material losses (such as free-carrier absorption) and scattering loss from imperfections in the lasers [32–35]. Surface defects on the sidewalls of optical cavities, introduced during the etching process, lead to unwanted surface recombination and additional optical loss, thereby increasing the threshold and decreasing the maximum lasing temperature of GeSn lasers [35]. Reducing sidewall roughness to suppress surface recombination is crucial for improving performance in terms of the threshold and maximum lasing temperature.

In this study, we demonstrate an optically pumped GeSn planar slab waveguide laser on a Si substrate with a Si-ridge structure on the GeSn gain medium. The incorporation of approximately 10% Sn into the GeSn active layer not only transforms the material into a direct bandgap material enabling efficient direct band-to-band transitions, but also shifts the emission wavelength to the MIR region, enhancing its utility for MIR silicon photonics. Our device design features a Si-ridge structure that forms guided modes with excellent optical confinement without etching the GeSn active layer, thereby minimizing the optical loss caused by surface defects. Lasing action was observed with a low threshold of 60.85 kW/cm^2 and an emission wavelength of 2238 nm at $T = 40$ K, and up to an operating temperature of 90 K with a threshold of 170 kW/cm^2.

2. Results and discussion

2.1. Device design and simulation

Figure 1(a) presents a 3D schematic of the proposed optically-pumped GeSn planar slab waveguide laser on a Si substrate. The GeSn sample comprises a 450 nm-thick strain-relaxed Ge virtual substrate (VS) and a 550 nm-thick GeSn active region containing 10% Sn on a Si (001) substrate. A 100 nm-thick amorphous Si ridge structure was engineered to form guiding modes without etching the GeSn active layer. As a result, surface non-radiative recombination caused by surface defects can be reduced, thereby suppressing optical losses and enhancing the laser's performance. To assess the optical confinement of the layers, finite element method (FEM) simulations were conducted using the refractive indices (RIs) of the materials by referring to previous studies [36,37] to determine the field distribution and the optical confinement factors (OCFs) for the various layers with different widths of the Si ridge layer. Figure 1(b) illustrates the simulated OCF as a function of the width of the amorphous Si layer (w) and the energy distribution for the quasi-transverse electric (TE) mode with $w = 20$ μm at $\lambda = 2200$ nm. The energy distribution reveals that the Si ridge structure and the Si substrate provide significant optical confinement for the GeSn active layer, which is attributable to the substantial contrast in RIs between GeSn ($n = 4.3$) and Si ($n = 3.45$). As shown in Fig. 1(b), the OCF for the GeSn active layer increases with the widening of the Si ridge, following a saturation trend. Consequently, a high OCF of 66.80% was achieved for the GeSn active layer, indicating robust optical confinement. Additionally, the guided mode is positioned far from the sidewall of the Si-ridge structure, suggesting minimized impact from sidewall defect-related recombination and reduced optical loss on the lasing action.

Optics EXPRESS

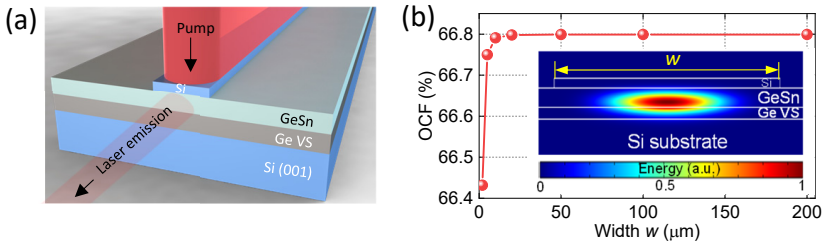

Fig. 1. Device design and simulation. (a) Schematic of the GeSn slab waveguide laser on Si substrate. (b) Simulated optical confinement factor (OCF) as a function of the width of amorphous Si top layer. The inset shows the simulated field distribution at $\lambda = 2200$ nm for the quasi-transverse electric fundamental mode.

2.2. *Material growth and characterization*

The sample used in this study was grown by reduced-pressure chemical vapor deposition (RPCVD) on a Si (001) substrate with Ge_2H_6 and $SnCl_4$ precursors for Ge and Sn, respectively. The epitaxial process included the growth of a strain-relaxed Ge VS using a two-step growth technique, and the growth of a GeSn layer at 320 °C to reduced Sn segregation. The material characterization was conducted using cross-sectional transmission electron microscopy (XTEM), secondary ion mass spectrometry (SIMS), selected area electron diffraction (SAED), X-ray reciprocal space mapping (RSM) and photoluminescence (PL) techniques. Figure 2(a) depicts the XTEM image alongside the SIMS depth profile showing the atomic distribution of Ge and Sn atoms. Misfit dislocations were evident in the Ge VS near the Si substrate, indicating that the Ge VS was strain-relaxed. Additionally, the XTEM image revealed sharp and flat interfaces between the Ge VS and GeSn active layers. The SIMS profile indicates a uniform distribution of Sn atoms within the GeSn layer. The inset in Fig. 2(a) shows the SAED image for the active GeSn layer, demonstrating its single-crystalline nature. The high-resolution XTEM image at the Ge/GeSn interface as shown in the inset of Fig. 2(a) provides clear evidence of high material quality. Figure 2(b) displays the X-ray RSM of the (224) plane. Three distinct peaks were identified, corresponding to the Si substrate, Ge VS, and GeSn active layer. The diagonally passing strain-relaxed line confirms that the Ge VS was tensile strained while the GeSn layer was compressively-strained. From the position of the diffraction peaks, the in-plane and out-of-plane lattice constants of the layers were extracted to determine the strain and composition. The analysis indicates that the Ge VS is subject to an in-plane biaxial tensile strain of 0.17% due to the difference in thermal expansion coefficients between Ge and Si during epitaxial growth [19]. In contrast, the GeSn layer exhibits an Sn concentration and in-plane biaxial compressive strain of 10% and 0.264%, respectively.

Temperature-dependent PL experiments were conducted using a 1064 nm continuous-wave laser as the pumping source and a Fourier transform infrared (FTIR) spectroscope equipped with an LN_2-cooled InSb photodetector operating in a 1-5 μm spectral range. Figure 2(c) illustrates the temperature-dependent PL spectrum of our sample. A strong emission signal peak at 2222 nm was observed at $T = 77$ K (corresponding to a photon energy of 0.558 eV). Compared with the direct-gap emission wavelength of approximately 1550 nm for pure Ge, the extension of emission wavelength was attributed to the incorporation of Sn in the GeSn layer. From the temperature-dependent PL spectra, the PL peak position as a function of temperature was depicted in Fig. 2(d). To clearly understand the effect of temperature on the direct bandgap of GeSn, we fitted the experimental data using the Varshni equation [38,39],

$$E_g^{\Gamma}(T) = E_g^{\Gamma}(T=0) - \frac{\alpha \times T^2}{T+\beta} \tag{1}$$

Optics EXPRESS

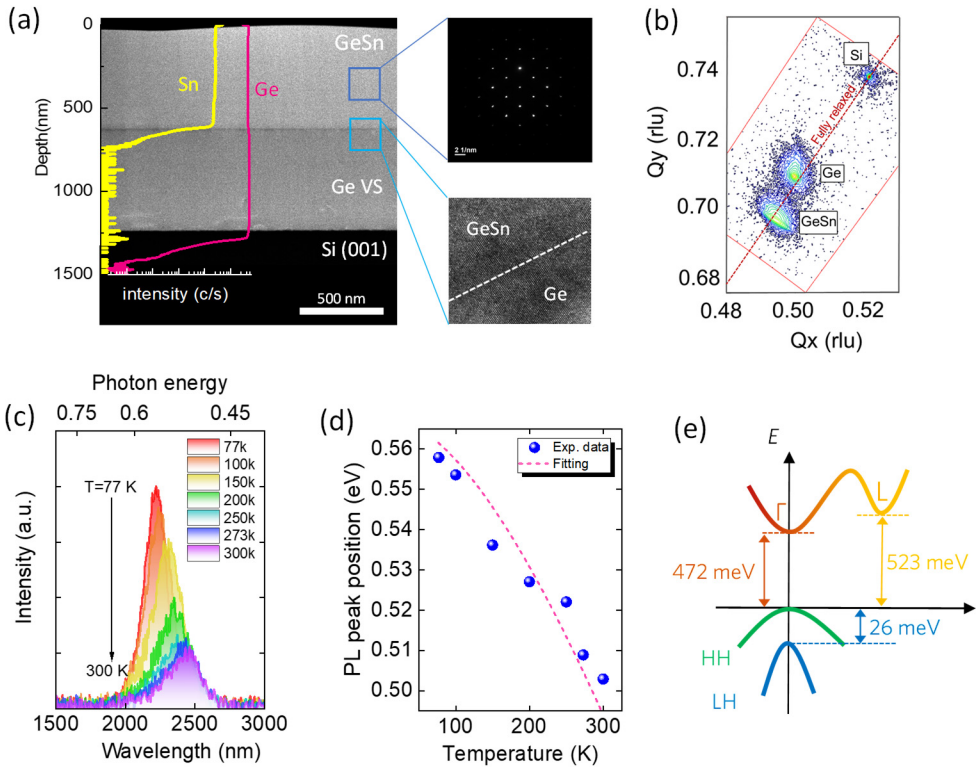

Fig. 2. Material characterization and analysis. (a) Cross-sectional transmission electron microscopy (XTEM) image with secondary ion mass spectrometry (SIMS) diagram of the atomic distribution of Ge and Sn atoms. The inset shows the selected area electron diffraction (SAED) pattern of the GeSn active layer and high-resolution XTEM image at the GeSn/Ge interface. (b) X-ray (224) reciprocal space mapping (RSM) of the sample used in this study. The dark red line represents full strain relaxation. (c) Temperature-dependent photoluminescence (PL) spectra of the GeSn sample. (d) PL peak position as a function of temperature with the Varshni fitting. (e) Calculated band structure of the GeSn active layer at $T = 77$ K.

where α and β are the Varshni parameters, $E_g^{\Gamma}(T = 0)$ is the direct bandgap energy at $T = 0$ K. From the fitting shown in Fig. 2(d), we obtained $\alpha = 7.05 \times 10^{-4}$ eV/K, β=559.73 K, and $E_g^{\Gamma}(T = 0\ \mathrm{K}) = 0.569$ eV, which are useful for estimating the direct bandgap energy of the GeSn alloy at various temperatures. To gain a deeper understanding of the emission peak, we theoretically calculated the electronic band structure of the GeSn active layer considering the strain effect via the multi-band k p method [38]. The calculated band structure of the GeSn active layer at $T = 77$ K is illustrated in Fig. 2(e). The results suggest that the introduction of 10% Sn in the GeSn active layer shifts the Γ-valley CB to be lower than the L-valley CB by 51 meV, highlighting the directness of the band structure. Furthermore, the compressive strain of approximately 0.264% breaks the degeneracy of the heavy hole (HH) and light hole (LH) bands in the valance band (VB), shifting the HH band above the LH band by approximately 26 meV. As a result, the lowest direct-band transition occurs when electrons jump from the Γ-valley CB to the HH band by releasing energy of ~562 meV which gives a good agreement of our experimental findings. This analysis proves that the observed emission was caused by the interband transition from the Γ-valley CB to the HH band (Γ→HH). When the temperature decreased, the PL emission peak redshits owing to the decreased bandgap energy. The PL

Optics EXPRESS

intensity also decreased with increasing temperature, which also indicates that the GeSn active layer is a direct bandgap material.

2.3. Optical characterization

The sample was fabricated into devices using CMOS-compatible processes. Mesas with a width of $w = 200$ μm were patterned by standard optical lithography followed by SF_4-based reactive ion etching (RIE) to form ridge-shaped waveguide structures. The sample was subsequently cleaved into devices of various lengths; the device used in this study measured a length of $L = 1.78$ mm. Scanning electron microscopy (SEM) image of the fabricated GeSn device is shown in Fig. 3(a).

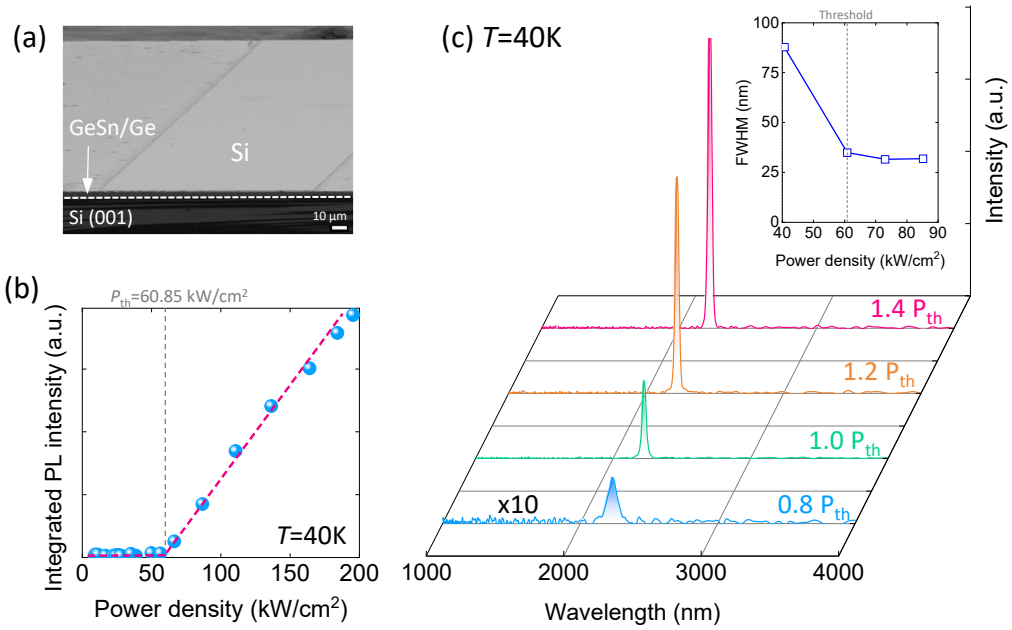

Fig. 3. Optical characterization of our GeSn laser. (a) Scanning electron microscope (SEM) image of the fabricated device. (b) Light-in-light-out (*L*-*L*) curve of the GeSn device at $T = 40$ K. The threshold is denoted by the grey dashed line. (c) Power-dependent emission spectra of the GeSn device at $T = 40$ K. The inset shows the full-width-at-half-maximum of the emission peak at various power densities.

PL experiments were conducted using a 1064 nm pulsed laser with a pulse width of 12 ns and a repetition rate of 12.5 kHz as the pumping light source, which was modulated using an optical chopper at a frequency of 200 Hz. The pumping laser was incident normally on the GeSn devices mounted in a cryogenic system through a cylindrical lens. The light emitted from one facet of the GeSn device was collected and analyzed using a FTIR. A special step-scan technique was adopted to enhance the signal-to-noise ratio and eliminate background thermal radiation. Figure 3(b) presents the light-in-light-out (*L*-*L*) curve of the GeSn device at $T = 40$ K. The PL intensity was low at a low pumping power intensity, where spontaneous emission dominated. Above a certain pumping power density, the PL intensity increased sharply, indicating that stimulated emission began to dominate the light emission. The onset of the *L*-*L* curve defines the threshold of the GeSn laser as $P_{th} = 60.85$ kW/cm^2. The obtained threshold of our GeSn lasers is lower than the typical values of 100–600 kW/cm^2 reported for optically pumped GeSn lasers on Si with Sn contents of 12–16% [12,13,19–21]. The lower threshold of our GeSn lasers is attributed to reduced loss from surface defects, highlighting the importance of our planar slab waveguide

Optics EXPRESS

design. Figure 3(c) exhibits the measured PL spectra at $T = 40$ K above and below the threshold. Fitting the emission peaks using the Gaussian function yielded the full-width-at-half-maximum (FWHM). The inset in Fig. 3(c) shows the FWHM extracted from the emission spectra as a function of the pumping density. Below the threshold, a broad and weak emission peak was observed at $\lambda = 2239$ nm with an FWHM of 87 nm (21.5 meV). Contrarily, when the pumping power density reaches the threshold, the intensity of the emission peak increased sharply with a narrowed FWHM of 35 nm (8.6 meV), comparable to the results reported for other GeSn optically pumped lasers [18,19]. As the pumping power intensity increased further, the intensity of the emission peak increased more significantly, and the FWHM sharply decreased, confirming linewidth narrowing. These results verify the achievement of lasing action from the developed GeSn lasers.

Next, we evaluated the temperature-dependent characteristics of the GeSn laser. Figure 4(a) illustrates the temperature-dependent PL spectra measured from our fabricated GeSn slab waveguide laser at different temperatures under an optical pumping density of 500 kW/cm^2. As the temperature increased from $T = 40$ K, robust lasing peaks were clearly observed up to $T = 90$ K. Beyond this temperature, the broadening of the emission spectra and the absence of a distinct lasing peak indicate that spontaneous emission predominated at higher operating temperatures. The corresponding *L*-*L* curves, shown in Fig. 4(b), also demonstrated the "turn-on" behavior up to $T = 90$ K. Therefore, the highest lasing temperature of our GeSn laser was determined to be 90 K. The *L*-*L* curves were used to determine the thresholds at different temperatures, as shown in Fig. 4(c). The threshold increased from 60.85 kW/cm^2 at $T = 40$ K to 170 kW/cm^2 at $T = 90$ K. This increase in temperature thermally excited the optically generated electrons from the Γ-valley to the L-valley in the CB, necessitating higher optical pumping to achieve lasing action as the temperature increased. From the temperature-dependent threshold, the characteristic temperature (T_0) of the laser, which is crucial for understanding the thermal stability, can be determined using [38]

$$P_{\text{th}}(T) = P_{\text{th}}(T_a) \times \exp\left(\frac{T - T_a}{T_0}\right) \tag{2}$$

where $P_{\text{th}}(T_a)$ is the threshold at $T = T_a$. Fitting the data using Eq. (1) yields a characteristic temperature of T_0 =51.6 K for our GeSn laser. Ideally, a higher T_0 is desirable for stable laser applications. A further increase in Sn content in the GeSn layer could enhance the directness of band structure and improves laser passivation, thereby enhancing laser performance.

Figure 5(a) presents a high-resolution scan of the emission spectrum at $T = 77$ K with a spectral resolution of 2 cm^{-1} (~0.5 nm) and a pumping power density of 146.85 kW/cm^2. As shown in the inset of Fig. 5(a), periodic peaks, as indicated by the arrows, were clearly observed, corresponding to the Fabry–Pérot longitudinal modes of the cavity, which suggests multiple-mode lasing. The peak wavelength positions of the cavity modes extracted from the emission spectrum are depicted in Fig. 5(b). A linear fit of the peak positions yielded a longitudinal mode spacing of 5.47 ± 0.22 nm. Additionally, fitting the emission peak with a Gaussian function yields a FWHM of approximately 6.2 nm, revealing narrow linewidth of the lasing modes.

We then examine the polarization behavior of the optically-pumped GeSn slab laser. The GeSn laser was optically-pumped at $T = 77$ K above the threshold (146.85 kW/cm^2). The lasing emission was filtered using a linear polarizer mounted on a motorized rotation stage to precisely control the polarization angle (θ). Figure 6(a) shows the emission spectra at various polarization angles. The emission intensity was strongest at θ=0°, and decreased with increasing polarization angle. Figure 6(b) shows the corresponding polar plot of the emission intensity. The emission intensity reaches a maximum (minimum) at θ=0° (θ=90°), indicating the TE component was dominant over the transverse magnetic (TM) component. This observation aligns with the calculated band structure of the GeSn active layer (Fig. 2(e)), where the Γ→HH transition is the lowest interband transition, leading to the generation of TE-polarized light [38]. The polarization

Optics EXPRESS

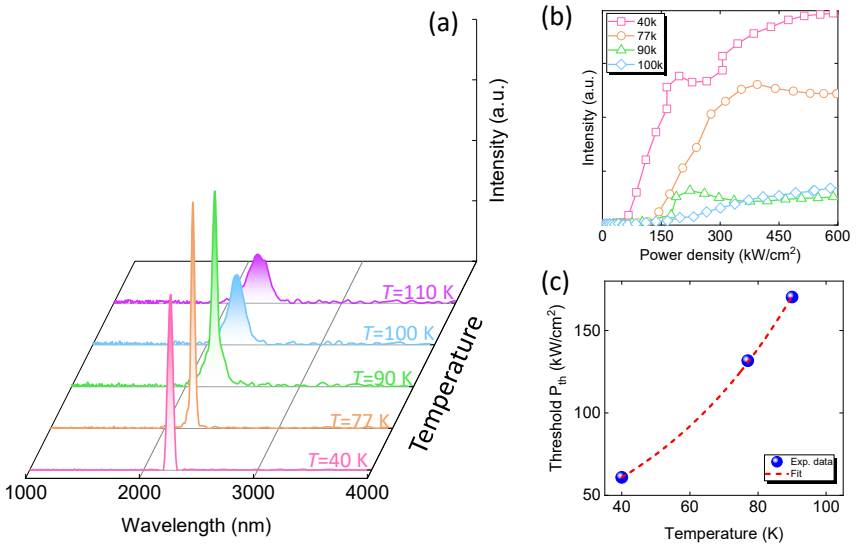

Fig. 4. Temperature-dependent optical characteristics**.** (a) Temperature-dependent PL spectra from our GeSn slab laser measured at various temperatures. (b) Measured *L*-*L* curves at various temperatures. (c) Extracted threshold power density as a function of temperature.

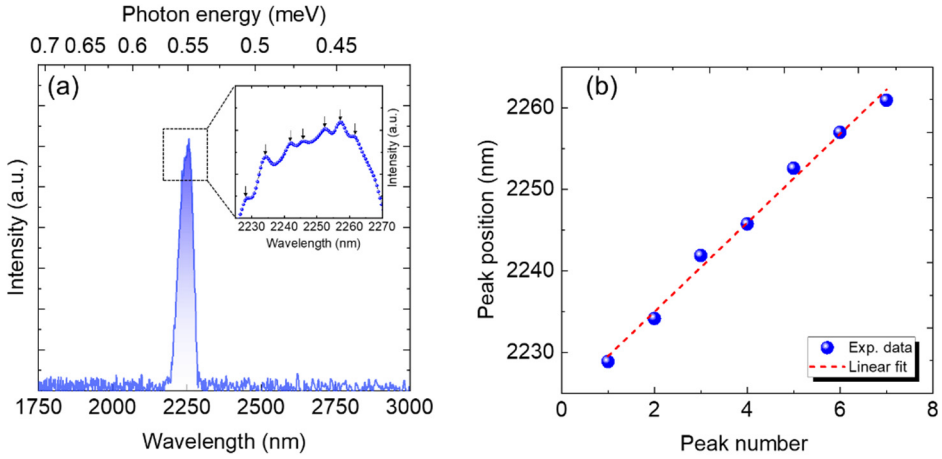

Fig. 5. (a) High-resolution scan of the emission spectrum at $T = 77$ K. The inset shows the enlarged part of the emission spectrum, with the emission peaks indicated by arrows. (b) Peak wavelength position versus cavity mode.

anisotropy can be characterized by $\rho = (I_{max} - I_{min})/(I_{max} + I_{min})$, where I_{max} and I_{min} are the maximum and minimum emission intensities, respectively. A high polarization anisotropy of $\rho = 97.5\%$ was obtained, indicating the lasing emission was almost linearly polarized.

Figure 7 shows a comparison between the threshold of our GeSn laser and previous optically-pumped GeSn lasers with Fabry–Pérot cavities [12,13,40–43] in terms of Sn composition and operating temperature. Among these optically-pumped GeSn lasers, our GeSn slab waveguide laser features a low threshold and/or a higher lasing temperature than the reported GeSn-based waveguide lasers with higher Sn contents. This can be attributed to the good material quality, good optical confinement, and reduced surface and sidewall recombination losses, highlighting

Optics EXPRESS

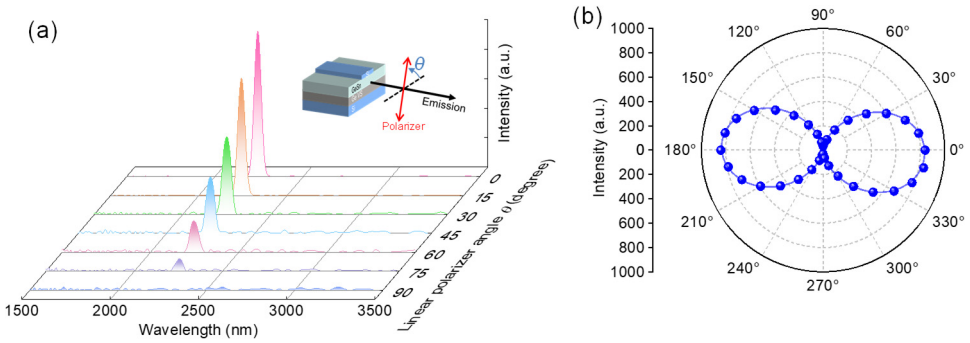

Fig. 6. Laser emission polarization characteristics. (a) Emission spectra at various polarization angles measured at $T = 77$ K. (b) The corresponding polar plot of the integrated emission intensity.

both the importance of our slab waveguide laser structure design and the competitiveness of our device. It is anticipated that increasing the Sn content in the GeSn layer could enhance the directness of the band structure and improve the threshold and/or increase the lasing temperature [29]. Additionally, the emission wavelength can be tuned in the MIR region by adjusting the Sn content, making it suitable for MIR silicon photonics.

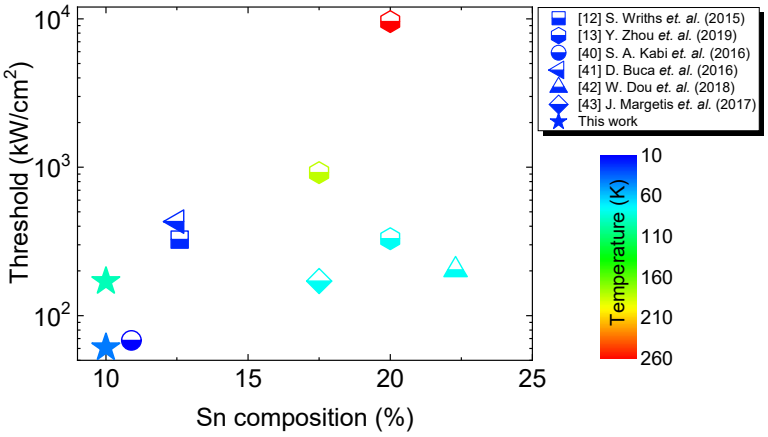

Fig. 7. Comparison of lasing threshold and temperature of optically pumped GeSn lasers with Fabry–Pérot cavities [12,13,40–43].

3. Conclusion

In conclusion, we have successfully demonstrated an optically pumped GeSn slab waveguide laser on a Si platform with a Si ridge structure. This planar GeSn laser structure, combined with the Si ridge, demonstrates excellent optical confinement within the active layer while minimizing overlap with the ridge structure's sidewall, thereby reducing optical loss and enabling efficient lasing action. With the incorporation of 10% Sn, the emission wavelength extends to 2254 nm. Lasing action was confirmed by the clear threshold behavior, linewidth narrowing, and TE dominant polarized emission. Additionally, this fabricated GeSn slab laser achieves a low threshold of 60.85 kW/cm^2 at $T = 40$ K and maintains effective lasing up to 90 K with a threshold of 170 kW/cm^2. The characteristic temperature of 51.6 K indicates the need for

Optics EXPRESS

further improvements to enhance thermal stability. These findings suggest that a highly credible GeSn laser with a lower threshold is achievable. By carefully designing and optimizing the laser structure to reduce surface recombination, decreasing the threshold further and achieving efficient lasing even at higher temperatures is feasible. These results demonstrate immense potential for efficient CMOS-compatible lasers on Si for mid-infrared photonics, paving the way for broader applications in areas such as environmental sensing, healthcare diagnostics, and telecommunications.

Funding. National Science and Technology Council of Taiwan (NSTC 112-2636-E-194-001, NSTC 113-2636-E-194-001); Taiwan Semiconductor Research Institute (JDP112-Y1-028, JDP113-Y1-044).

Disclosures. The authors declare that there are no conflicts of interest related to this article.

Data availability. Data underlying the results presented in this paper may be available from the corresponding author upon reasonable request.

References

1. R. Soref, "The past, present, and future of silicon photonics," IEEE J. Select. Topics Quantum Electron. **12**(6), 1678–1687 (2006).
2. R. Soref, "Mid-infrared photonics in silicon and germanium," Nat. Photonics **4**(8), 495–497 (2010).
3. T. Hu, B. Dong, X. Luo, *et al.*, "Silicon photonic platforms for mid-infrared applications," Photonics Res. **5**(5), 417–430 (2017).
4. J. P. Gupta, N. Bhargava, S. Kim, *et al.*, "Infrared electroluminescence from GeSn heterojunction diodes grown by molecular beam epitaxy," Appl. Phys. Lett. **102**(25), 251117 (2013).
5. M. Bauer, J. Taraci, J. Tolle, *et al.*, "Ge-Sn semiconductors for band-gap and lattice engineering," Appl. Phys. Lett. **81**(16), 2992–2994 (2002).
6. A. V. G. Chizmeshya, C. Ritter, J. Tolle, *et al.*, "Fundamental studies of $P(GeH_3)_3$, $As(GeH_3)_3$, and $Sb(GeH_3)_3$: practical n-dopants for new group IV semiconductors," Chem. Mater. **18**(26), 6266–6277 (2006).
7. J. Liu, J. Michel, and L. C. Kimerling, "High-performance Ge-on-Si photodetectors," Nat. Photonics **4**(8), 527–534 (2010).
8. G. E. Chang, S. Q. Yu, J. Liu, *et al.*, "Achievable performance of uncooled homojunction GeSn mid-infrared photodetectors," IEEE J. Select. Topics Quantum Electron. **28**(2: Optical Detectors), 3800611 (2022).
9. Y. Zhou, S. Ojo, C. W. Wu, *et al.*, "Electrically injected GeSn lasers with peak wavelength up to 2.7 μm," Photonics Res. **10**(1), 222–229 (2022).
10. T. T. McCarthy, Z. Ju, S. Schaefer, *et al.*, "Momentum (k)-space carrier separation using SiGeSn alloys for photodetector applications," J. Appl. Phys. **130**(22), 223102 (2021).
11. S. Ghosh, G. Sun, S. Q. Yu, *et al.*, "Impact of carrier momentum (k)-space separation on GeSn infrared photodetectors," IEEE J. Select. Topics Quantum Electron. **31**(1), 3800211 (2025).
12. S. Wirths, R. Geiger, N. von den Driesch, *et al.*, "Lasing in direct-bandgap GeSn alloy grown on Si," Nat. Photonics **9**(2), 88–92 (2015).
13. Y. Zhou, W. Dou, W. Du, *et al.*, "Optically pumped GeSn lasers operating at 270 K with broad waveguide structures on Si," ACS Photonics **6**(6), 1434–1441 (2019).
14. J. Chretien, N. Pauc, F. A. Pilon, *et al.*, "GeSn lasers covering a wide wavelength range thanks to uni-axial tensile strain," ACS Photonics **6**(10), 2462–2469 (2019).
15. A. Elbaz, D. Buca, N. von den Driesch, *et al.*, "Ultra-low-threshold continuous-wave and pulsed lasing in tensile-strained GeSn alloys," Nat. Photonics **14**(6), 375–382 (2020).
16. H. J. Joo, Y. Kim, D. Burt, *et al.*, "1D photonic crystal direct bandgap GeSn-on-insulator laser," Appl. Phys. Lett. **119**(20), 201101 (2021).
17. G. Abernathy, S. Ojo, J. M. Grant, *et al.*, "Study of critical optical confinement factor for GeSn-based multiple quantum well lasers," Appl. Phys. Lett. **121**(17), 171101 (2022).
18. Y. Kim, S. Assali, D. Burt, *et al.*, "Enhanced GeSn microdisk lasers directly released on Si," Adv. Opt. Mater. **10**(2), 2101213 (2022).
19. D. Stange, S. Wirths, R. Geiger, *et al.*, "Optically pumped GeSn microdisk lasers on Si," ACS Photonics **3**(7), 1279–1285 (2016).
20. V. Reboud, A. Gassenq, N. Pauc, *et al.*, "Optically pumped GeSn micro-disks with 16% Sn lasing at 3.1 μm up to 180 K," Appl. Phys. Lett. **111**(9), 092101 (2017).
21. Q. M. Thai, N. Pauc, J. Aubin, *et al.*, "2D hexagonal photonic crystal GeSn laser with 16% Sn content," Appl. Phys. Lett. **113**(5), 051104 (2018).
22. Q. M. Thai, N. Pauc, J. Aubin, *et al.*, "GeSn heterostructure micro-disk laser operating at 230 K," Opt. Express **26**(25), 32500–32508 (2018).
23. A. Bjelajac, M. Gromovyi, E. Sakat, *et al.*, "Up to 300 K lasing with GeSn-on-insulator microdisk resonators," Opt. Express **30**(3), 3954–3961 (2022).

Optics EXPRESS

24. J. Chretien, Q. M. Thai, M. Frauenrath, *et al.*, "Room temperature optically pumped GeSn microdisk lasers," Appl. Phys. Lett. **120**(5), 051107 (2022).
25. Y. Zhou, Y. Miao, S. Ojo, *et al.*, "Electrically injected GeSn lasers on Si operating up to 100 K," Optica **7**(8), 924–928 (2020).
26. S. Amoah, S. Ojo, H. Tran, *et al.*, "Electrically injected GeSn laser on Si operating up to 110 K," *2021 Conference on Lasers and Electro-Optics (CLEO)*, 2021.
27. B. Marzban, L. Seidel, T. Liu, *et al.*, "Strain engineered electrically pumped SiGeSn microring lasers on Si," ACS Photonics **10**(1), 217–224 (2023).
28. S. Acharya, H. Stanchu, R. Kumar, *et al.*, "Electrically Injected mid-infrared GeSn laser on Si operating at 140 K," IEEE J. Select. Topics Quantum Electron. **31**(1), 1500507 (2025).
29. K. O. Arslan, R. Aksakal, and B. Cakmak, "Comparative results of 980 nm InGaAs/GaAs and 1550 nm AlGaInAs/InP diode lasers," Mater. Today: Proc. **46**, 7015–7020 (2021).
30. Z. Ning, H. Dong, Z. Jia, *et al.*, "InP/InGaAs/AlGaAs quantum-well semiconductor laser with an InP based 1550 nm n-GaAsSb single waveguide structure," AIP Adv. **13**(7), 075109 (2023).
31. Z. Qiao, X. Li, J. X. B. Sia, *et al.*, "Modal gain characteristics of a two-section InGaAs/GaAs double quantum well passively mode-locked laser with asymmetric waveguide," Sci. Rep. **12**(1), 5010 (2022).
32. S. Ghosh and G. E. Chang, "Theoretical Analysis of Threshold Characteristics in Electrically-Driven GeSn Lasers," IEEE J. Sel. Quantum Electron., (In press).
33. D. Baek, S. Rouvimov, B. Kim, *et al.*, "Surface recombination velocity of silicon wafers by photoluminescence," Appl. Phys. Lett. **86**(11), 112110 (2005).
34. F. Toor, D. L. Sivco, H. E. Liu, *et al.*, "Effect of waveguide sidewall roughness on the threshold current density and slope efficiency of quantum cascade lasers," Appl. Phys. Lett. **93**(3), 031104 (2008).
35. A. Elbaz, R. Arefin, E. Sakat, *et al.*, "Reduced lasing thresholds in GeSn microdisk cavities with defect management of the optically active region," ACS Photonics **7**(10), 2713–2722 (2020).
36. H. Tran, W. Du, S. A. Ghetmiri, *et al.*, "Systematic study of $Ge_{1-x}Sn_x$ absorption coefficient and refractive index for the device applications of Si-based optoelectronics," J. Appl. Phys. **119**(10), 103106 (2016).
37. E. D. Palik, *Handbook of Optical Constants of Solids*, Academic: Orlando, FL, USA (1985).
38. S. L. Chuang, *Physics of Photonics Devices*, 2nd Ed., Wiley, USA (2009).
39. G. E. Chang, S. Q. Yu, and G. Sun, ""GeSn Rule-23" – The performance limit of GeSn infrared photodiodes," Sensors **23**(17), 7386 (2023).
40. S. Al-Kabi, S. A. Ghetmiri, J. Margetis, *et al.*, "An optically pumped 2.5 μm GeSn laser on Si operating at 110 K," Appl. Phys. Lett. **109**(17), 171105 (2016).
41. D. Buca, N. von den Driesch, D. Stange, *et al.*, "GeSn lasers for CMOS integration," *IEEE International Electron Devices Meeting (IEDM)* 22.3.1–22.3.4 (2016).
42. W. Dou, Y. Zhou, J. Margetis, *et al.*, "Optically pumped lasing at 3 μm from compositionally graded GeSn with tin up to 22.3%," Opt. Lett. **43**(19), 4558–4561 (2018).
43. J. Margetis, S. Al-Kabi, W. Du, *et al.*, "Si-Based GeSn lasers with wavelength coverage of 2–3 μm and operating temperatures up to 180 K," ACS Photonics **5**(3), 827–833 (2018).